Enhanced Oxygen Reduction Activity on Ruddlesden−Popper Phase Decorated La$_{0.8}$Sr$_{0.2}$FeO$_{3−\delta}$ 3D Heterostructured Cathode for Solid Oxide Fuel Cells

Tao Hong,[†,‡] Mingyang Zhao,[‡] Kyle Brinkman,[‡] Fanglin Chen,[§] and Changrong Xia*,[†]

[†]CAS Key Laboratory of Materials for Energy Conversion, Department of Materials Science and Engineering, University of Science and Technology of China, Hefei, Anhui 230026, China

[‡]Department of Materials Science and Engineering, Clemson University, Clemson, South Carolina 29634, United States

[§]Department of Mechanical Engineering, University of South Carolina, Columbia, South Carolina 29208, United States

S *Supporting Information*
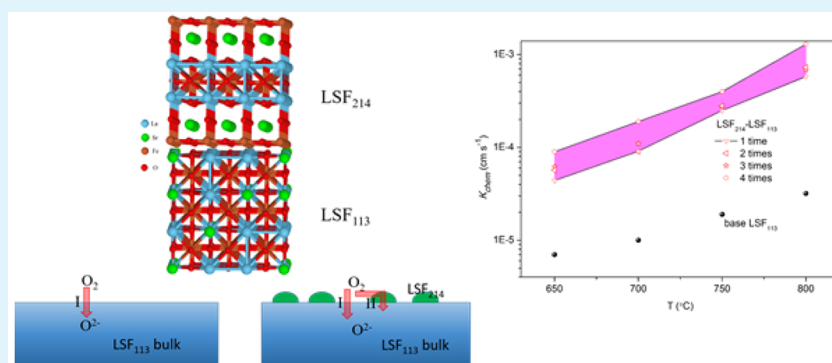
ABSTRACT: A new heterostructured (La,Sr)$_2$FeO$_{4−\delta}$ (LSF$_{214}$)-La$_{0.8}$Sr$_{0.2}$FeO$_{3−\delta}$ (LSF$_{113}$) electrode has been synthesized to improve the oxygen reduction reaction (ORR). This new materials system was fabricated by the deposition of Sr(NO$_3$)$_2$ into the LSF$_{113}$ framework followed by subsequent heat treatment, resulting in a new three-dimensional (3D) LSF$_{214}$-LSF$_{113}$ heterostructured electrode. This material system consists of a with Ruddlesden−Popper (R−P) LSF$_{214}$ phase formed on the surface of the LSF$_{113}$ framework. The ORR activity has been enhanced by 1 order of magnitude using the LSF$_{214}$-LSF$_{113}$ heterostructured electrode. The ORR enhancement was the result of higher catalytic activity of the LSF$_{214}$ phase and a mismatch in the lattice parameter between LSF$_{214}$ and LSF$_{113}$ regions which results in oxygen molecule adsorption and oxygen vacancy formation become more favored. Impedance spectroscopy measurements revealed that the presence of LSF$_{214}$ reduced the polarization resistance of the LSF$_{113}$ electrode on a ceria-based electrolyte. The high frequency resistance (R_H) and low frequency resistance (R_L) decreased substantially due to the enhanced oxygen transport process and accelerated oxygen incorporation rate in the LSF$_{214}$-LSF$_{113}$ heterostructured electrode. The heterostructured LSF$_{214}$-LSF$_{113}$ electrode provides a promising new approach to improve the oxygen reduction reaction activity through multiphase materials systems with tailored microstructures.

KEYWORDS: *oxygen reduction reaction, oxygen surface exchange, Ruddlesden−Popper phase, lanthanum strontium ferrite, solid oxide fuel cell*

INTRODUCTION

The cathode of solid oxide fuel cell (SOFC) provides reaction sites to catalytically reduce oxygen to oxygen anions.[1] Inadequate electrocatalytic activity of the cathode is still a major obstacle to advance low-temperature SOFCs. Both experimental and modeling studies have shown that oxygen surface process plays a dominant role in the oxygen reduction reaction (ORR).[2] The main challenge to achieving acceptable chemical to electrical conversion efficiency in SOFC is the sluggish ORR kinetics on the cathode.[3] Transition metal oxides with the perovskite structure possess a rich variety of properties originating from the mutual coupling between spin, charge, and lattice degrees of freedom.[4] Moreover, the capability of

tolerating large oxygen or cation nonstoichiometry in their lattice enables tailoring the perovskite structured oxides into high performance cathodes.[4]

Many studies have revealed that the creation of a new surface will break the symmetry of a crystal and thus induce various electronic, magnetic, and geometrical changes.[5] As a result of the transition of the surface, the surface free energy will be different from that of the bulk, inducing surface segregation and therefore changing the chemical composition of the surface

region.[6] Of particular interest are the heterostructures as they offer symmetric boundary conditions and a high density of heterointerfaces. Heterostructured interfaces of oxides, which can exhibit transport and reactivity characteristics remarkably different from those of the bulk oxides, are interesting systems to explore for high active cathodes for ORR. The field of ionic heterostructures has already been characterized by a variety of results of fundamental importance and of technological relevance.[5,7,8]

In design of heterostructured cathode, surface decoration of the conventional cathode materials with secondary phases has been shown to be a promising strategy to enhance ORR kinetics and cathode performance.[9] A highly active secondary phase such as a Ruddlesden−Popper phase[9,10] has been reported to form at the cathode surface that can drastically enhance the ORR activity. Previous studies have found that there are fast oxygen-incorporation paths along the heterophase boundary of $(La,Sr)_2CoO_{4−\delta}$ $(LSC_{214})/La_{0.8}Sr_{0.2}CoO_{3−\delta}$ (LSC_{113}) using secondary ion mass spectrometry, and such heterostructure can significantly enhance the kinetics of surface oxygen exchange.[11−13] Using electrochemical impedance spectroscopy measurements, Crumlin et al. have reported an ORR activity enhancement of 103−104 times at 550 °C on the thin film LSC_{113} cathodes whose surfaces are decorated with LSC_{214} islands (and thus with a high density of LSC_{113}/LSC_{214} interface).[10] Gadre et al.[14] have used density functional theory (DFT)-based simulations to demonstrate that Sr enrichment in LSC_{214} is expected to enhance the oxygen vacancy concentration by 2−2.5 orders of magnitude under typical experimental conditions. An increased oxygen vacancy concentration in LSC_{214} near the LSC_{113} interface can explain most of the enhanced oxygen kinetics observed in these heterostructures.

Mutoro et al.[9] used pulsed laser deposition (PLD) to deposit Sr on LSC film surface and found that "Sr" decoration with nanoparticle coverage in the range from 50% to 80% of the LSC surface enhanced the oxygen surface exchange coefficient (K_{chem}) by 1 order of magnitude. The enhanced K_{chem} is due to the formed $(La,Sr)_2CoO_{4−\delta}$ phase between SrO and $La_{0.8}Sr_{0.2}CoO_{3−\delta}$ film. However, it seems that the heterostructured thin films can only be prepared on the flat substrate by physical vapor deposition such as molecular beam epitaxy (MBE) and PLD.[5] Moreover, only two-dimensional (2D) heterostructures have been obtained from the physical vapor deposition technique, and the overall process is complex and costly. Other methods to synthesize core−shell particles such as the coprecipitation method, assembly process, and templating method[15,16] can also be used to produce heterostructured oxides. On the other hand, the microstructure of electrode is also an important factor for the cathode electrochemical performance. A nanoporous morphology is preferred since such microstructures have large effective surface areas for the electrocatalytic reactions, leading to lower cathodic overpotentials.

Here we report a novel 3D heterostructured cathode, consisting of stoichiometric $La_{0.8}Sr_{0.2}FeO_{3−\delta}$ (LSF_{113}) as the core and concentration graded $(La,Sr)_2FeO_{4−\delta}$ (LSF_{214}) as the shell, prepared by infiltrating $Sr(NO_3)_2$ solution into porous LSF_{113} backbone followed by heat treatment. Electrical conductivity relaxation experiments revealed that the oxygen reduction activity of the LSF_{113} electrode was drastically enhanced by LSF_{214} nanoislands on the LSF_{113} surface. The higher oxygen catalytic activity of LSF_{214} and mismatch in

lattice parameter promoted the oxygen incorporation process. In the LSF_{214}-LSF_{113} electrode, the polarization resistance was reduced due to the enhanced oxygen ion transport rate and accelerated oxygen surface reduction process. Single cell testing was employed to examine the electrochemical performance of the LSF_{214}-LSF_{113} heterostructured cathode in an operational solid oxide fuel cell.

■ METHODS AND MATERIALS

Powder Synthesis and Sample Preparation. LSF_{113} $(La_{0.8}Sr_{0.2}FeO_{3−\delta})$ and LSF_{214} $(La_{0.8}Sr_{1.2}FeO_{4−\delta})$ powers were made by glycine−nitrate and glycine−citrate method, respectively. To synthesize LSF_{113}, stoichiometric amounts of precursors $La(NO_3)_3$, $Sr(NO_3)_2$, and $Fe(NO_3)_3$ (Sinopharm Chemical Reagent Co. Ltd.) were dissolved in distilled water. Glycine was then added to the solution at a mole ratio of 1:2 for glycine: nitrate ions. To synthesize LSF_{214}, besides the precursors as used in LSF_{113}, citrate of half amount of the glycine was also added. The precursor solution was subsequently heated on a hot plate until self-combustion occurred. The resulting ashes were calcined at 700 °C for 2 h to remove possible organic residues and to form the desired crystalline phase. The calcination temperature for LSF_{214} is 1100 °C. SDC $(Sm_{0.2}Ce_{0.8}O_{2−\delta})$, YSZ $(Y_{0.15}Zr_{0.85}O_{2−\delta})$, and NiO were also prepared with glycine−nitrate process and formed by firing the ashes at 850 °C for 4 h.

In the electrical conductivity relaxation (ECR) experiment, the LSF_{113} powders were ground, pressed into a rectangular bar at 300 MPa, and sintered at 1450 °C for 5 h in air to form dense LSF_{113} samples. The sintered LSF_{113} bars have a dimension of 35.00 mm × 5.42 mm × 0.90 mm. An appropriate amount of $Sr(NO_3)_2$ and glycine was dissolved in water with the metal ion concentration of 0.3 mol $L^{−1}$ to prepare the infiltration solution. Then the infiltrating $Sr(NO_3)_2$ solution was dropped onto the surface of the sintered LSF_{113} bars and then fired at 800 °C for 2 h. For different samples, the bars were gone through 1−4 times infiltration treatment, and after each thermal treatment (800 °C for 2 h), the bars were ultrasonically cleaned in water and ethanol separated for 10 min.

Symmetrical half-cells consisting of dense SDC electrolyte and porous LSF electrodes were fabricated for electrochemical test. The SDC powders were uniaxially pressed at 250 MPa to form green pellets with a diameter of 13 mm. The SDC pellets were subsequently sintered at 1350 °C for 5 h. LSF_{113} slurry was prepared by mixing LSF_{113} powders with organics (α-terpineol as solvent and ethyl cellulose as the binder) and then printed onto both sides of the sintered SDC pellets. After drying under an infrared lamp, the symmetrical half-cells were fired at 1100 °C for 2 h. To fabricate the 3D heterostructure, ion impregnation was carried out by placing a drop of $Sr(NO_3)_2$ solution as used in ECR experiment on the top of the porous LSF_{113} layer, letting the solution soak into the porous LSF_{113} backbone, drying, and then firing the sample at 800 °C in air for 2 h. The mass of the sample before and after each impregnation treatment was measured to estimate the solid loading of the impregnated material.

Anode supported single cells have a cell configuration of Ni-YSZ anode substrates, YSZ/SDC thin film electrolytes, and LSF cathodes. The anode powders consisting of 60 wt % NiO and 40 wt % YSZ were mixed, and 20 wt % PMMA was added as the pore former. The anode powders were pressed at 30 MPa and then fired in air at 800 °C for 2 h. YSZ slurry was then dip coated on the top of the NiO-YSZ pellet. The NiO-YSZ/YSZ bilayers were sintered at 1400 °C for 5 h to densify the electrolyte layer. SDC slurry was subsequently dip coated in the YSZ electrolyte surface, dried, and then sintered at 1100 °C for 2 h. SDC slurry was then infiltrated into the SDC layer, dried, and sintered at 1250 °C for 5 h to densify the SDC layer. The LSF cathode was fabricated on top of the SDC layer with the same process as that for the symmetrical half-cells.

Sample Characterization. The crystalline phase of the samples was investigated using X-ray diffraction (XRD, Rigaku TTR-III diffractometer) with Cu Kα radiation source. The XRD patterns were obtained in the range of 20°−80° with a 0.02° step size and a

scan speed of 0.5°/min at 40 kV and 200 mA. In LSF$_{214}$-LSF$_{113}$ XRD measurement, porous 8.75 wt % electrode supported by SDC electrolyte pellet was directly used on a glass sample holder. Oxygen nonstoichiometry coefficient and crystalline parameters were calculated from the XRD data using the Rietveld refinement method. Thermal gravimetric analysis (TGA) and isothermal gravimetric measurement were carried out using a thermal analyzer (Shimadzu DGT-60H) in 75 mL min^{-1} dry air atmosphere. The morphology of the LSF$_{214}$-LSF$_{113}$ electrode was characterized using scanning electron microscopy (SEM, JEOL JSM-6700F) and atomic force microscopy (AFM, SPA-300HV and Nanoscope software). The 8.75 wt % LSF$_{214}$-LSF$_{113}$ electrode was scraped from SDC electrolyte pellet and then dispersed in ethanol by ultrasonic to prepare sample for transmission electron microscopy (TEM, JEOL JSM-2010).

X-ray photoelectron spectroscopy (XPS, thermo ESCALAB250) was used to determine the surface compositions of the infiltrated electrode. Survey spectra with low and high resolution of La 3d (RSF as supplied by the XPS manufacturer: 9.122), Sr 3d (RSF: 1.843), Fe 2p (RSF: 14.8912), O 1s (RSF: 0.780), and C 1s (RSF: 0.278) were collected at room temperature and a base pressure of $\approx 10^{-8}$ mbar. The binding energy, E_{bind}, was calibrated to the C 1s photoemission peak of adventitious hydrocarbons at 285 eV.

Electrical and Electrochemical Testing. An electrical conductivity relaxation (ECR) experiment was used to determine the oxygen diffusion coefficient (D_{chem}) and oxygen chemical surface exchange coefficient (K_{chem}). The conductivity of LSF$_{113}$ bars used for the ECR test was measured by a standard, four-probe method using a measurement system consisting of a digital multimeter (Keithley 2001) interfaced with a computer and a program written using the LABVIEW 8.5 software. The atmosphere is changed from $P_{O_2} = 0.1$ bar ($O_2 + N_2$) to $P_{O_2} = 0.21$ bar ($O_2 + N_2$), and the details of the experiment have been described previously.[14] The change in conductivity of the sample with time is plotted as $(\sigma(t) - \sigma(0))/(\sigma(\infty) - \sigma(0))$, where $\sigma(0)$, $\sigma(t)$, and $\sigma(\infty)$ denote the initial, time-dependent, and final conductivities, respectively. The experimental data are fitted to the theoretical equations as outlined by Lane and Kilner[15] for conductivity relaxation to derive the oxygen surface exchange and the oxygen diffusion coefficients.

The electrochemical impedance spectra (EIS) of the symmetric half-cells were obtained using a Zahner (im6e) electrochemical workstation. The frequency range was from 0.1 Hz to 1 MHz, and the signal amplitude was 10 mV under open cell voltage conditions. A porous Ag counter electrode was attached with Ag silver as the lead wire. Zview software (Scribner Associates) was utilized to construct the equivalent circuit, correlate the electrode system with the EIS response, and perform complex least-squares fitting. The coin-shaped single cell was mounted onto an alumina tube and sealed by silver paste. H$_2$ with 3 vol % H$_2$O was fed into the anode side as the fuel at a flow rate of 20 mL min^{-1} while the cathode side was exposed to air. The current−voltage curves of the fuel cells operated between 650 and 800 °C were obtained. The cell ohmic and polarization resistances were also obtained from the EIS test.

■ RESULTS AND DISCUSSION

Chemistry of LSF$_{113}$ and LSF$_{214}$ Phases. Figures 1a and 1e show the XRD patterns of LSF$_{113}$ and LSF$_{214}$, respectively. Bare LSF$_{113}$ displays a perovskite structure. However, when mixed with Sr(NO$_3$)$_2$ and sintered at 800 °C for 2 h, LSF$_{113}$ reacted with Sr(NO$_3$)$_2$ during the heat-treatment process to form a Ruddlesden−Popper phase LSF$_{214}$ (La$_{0.8}$Sr$_{0.2}$FeO$_{3-\delta}$ + SrO → La$_{0.8}$Sr$_{1.2}$FeO$_{4-\delta}$). Figures 1b−d are the XRD patterns of mixtures of Sr(NO$_3$)$_2$ and La$_{0.8}$Sr$_{0.2}$FeO$_{3-\delta}$ at a mole ratio of 0.1:1, 0.3:1, and 0.6:1. In Figure 1b, there are very weak peaks in the range $2\theta = 31.3°$ (103) and 32.8° (110). Increasing the amount of Sr(NO$_3$)$_2$, the peak intensity of LSF$_{214}$ increases continuously because increased Sr(NO$_3$)$_2$ content leads to the formation of additional LSF$_{214}$. Previous studies have also
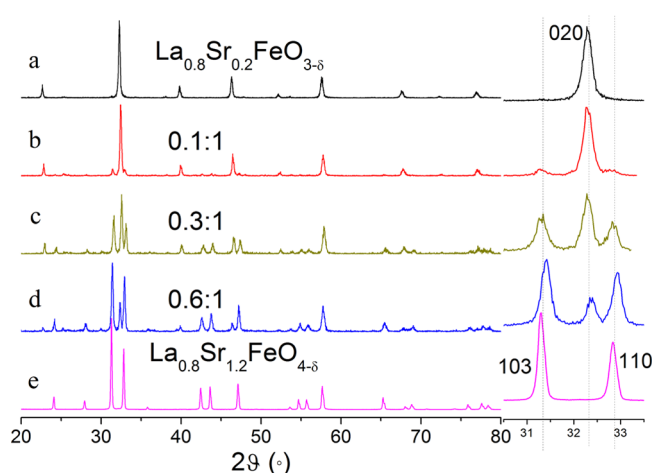

Figure 1. XRD patterns for (a) LSF$_{113}$ powder heated at 800 °C for 2 h, (b−d) Sr(NO$_3$)$_2$ mixed with LSF$_{113}$ at mole ratio of 0.1:1, 0.3:1, and 0.6:1 and heated at 800 °C for 2 h, and (e) bare LSF$_{214}$ powder heated at 1100 °C for 2 h.

Table 1. Lattice Parameter of LSF$_{113}$ and LSF$_{214}$ Powders Derived from XRD Rietveld Analysis

sample	a (Å)	b (Å)	c (Å)	δ
LSF$_{113}$	5.547	5.526	7.821	0.001
LSF$_{214}$	3.852	3.852	12.751	0.02

revealed surface restructuring and formation of a surface Ruddlesden−Popper phase ((La,Sr)$_2$MnO$_4$, (La,Sr)$_2$CoO$_4$, and Sr$_2$TiO$_4$) in other Sr-containing perovskites such as La$_{0.65}$Sr$_{0.35}$MnO$_3$, La$_{0.8}$Sr$_{0.2}$CoO$_3$ and SrTiO$_3$.[6,9,19] The magnified peaks from 30.5° to 33.5° are also provided in Figure 1. The (020) peak, characteristic of LSF$_{113}$, decreases while the (103) and (110) peaks characteristic of LSF$_{214}$ increase with increasing amount of Sr(NO$_3$)$_2$. These results demonstrate the formation of the LSF$_{214}$ phase in the LSF$_{113}$ phase scaffold and the compatibility in the LSF$_{214}$-LSF$_{113}$ heterostructure.

To investigate the crystalline structure difference between LSF$_{113}$ and LSF$_{214}$, Rietveld refinements of the XRD data were performed using the perovskite and K$_2$NiF$_4$ type crystalline structure as shown in Figure S1.[20] The a, b, and c unit-cell parameters as well as oxygen nonstoichiometry, δ, of LSF$_{113}$ and LSF$_{214}$ are shown in Table 1. The variation in the unit-cell constants is due to the crystalline structure. Consistent with the lattice parameters reported by Skinner et al.[21] and Omata et al.,[22] the a and b parameters for LSF$_{113}$[23] are 5.547 and 5.526 Å, which are much larger than 3.852 and 3.852 Å for LSF$_{214}$. Because of the added SrO rock-salt slabs in LSF$_{214}$, the c parameter increases greatly from 7.821 Å (in LSF$_{113}$) to 12.75 Å (in LSF$_{214}$). Rietveld refinements also indicate that there is a small amount of oxygen loss in both LSF$_{113}$ and LSF$_{214}$, leading to an overall oxygen deficiency of $\delta = 0.001$ and 0.02 in LSF$_{113}$ and LSF$_{214}$, respectively. Oxide cathode would commonly show weight loss at elevated temperatures. In order to investigate the oxygen nonstoichiometry, the weight change of LSF$_{113}$ and LSF$_{214}$ was compared as a function of temperature. The TGA result (Figure S2) reveals a 2.95% weight loss for LSF$_{113}$ and a 9.96% weight loss for LSF$_{214}$ from 50 to 850 °C. The weight loss is due to the loss of lattice oxygen, and higher weight loss at elevated temperature indicates formation of more oxygen vacancies in the oxide lattice.
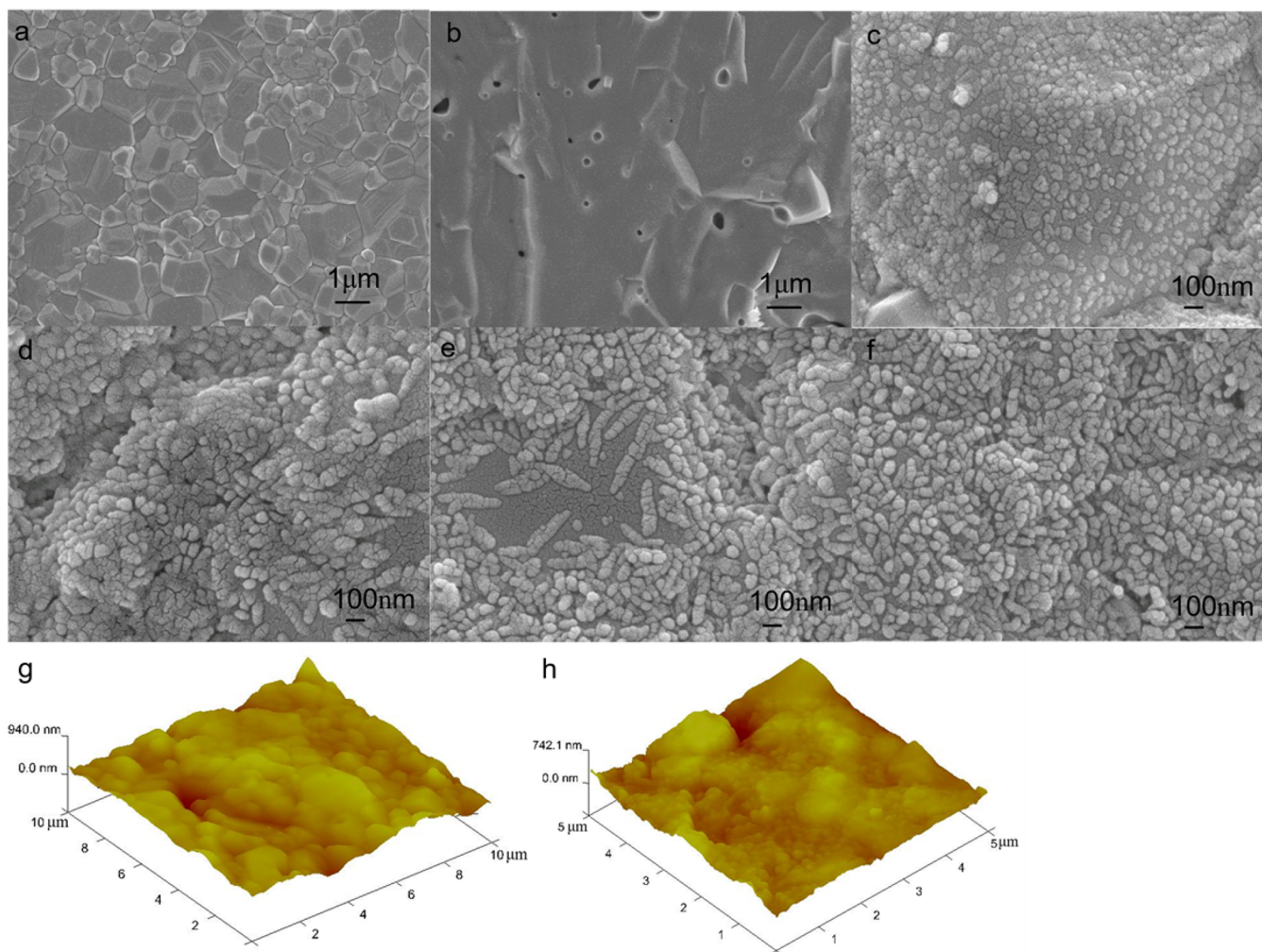
Figure 2. SEM pictures LSF_{113} and LSF_{214}-LSF_{113} samples after ECR testing: (a) surface and (b) cross section of bare LSF_{113}, and (c−f) LSF_{214}-LSF_{113} surface with different amount of LSF_{214} nanoisland after 1−4 times infiltrating treatment. AFM image of (g) bare LSF_{113} and (h) LSF_{214}-LSF_{113} as the same sample in (f).

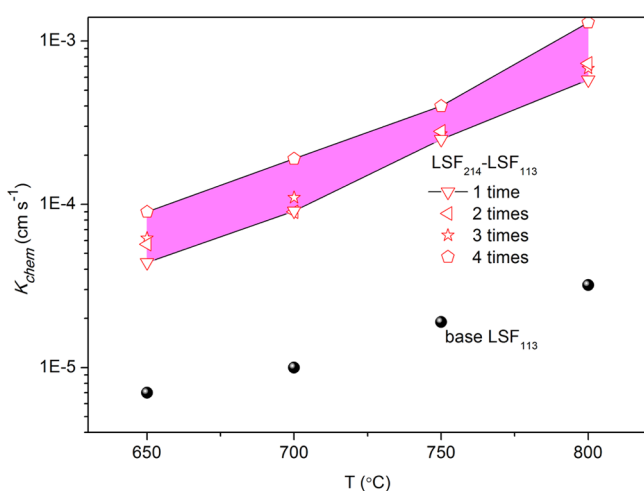**Figure 3.** Comparison of surface exchange coefficient, K_{chem}, for bare LSF_{113} and LSF_{214}-LSF_{113}.
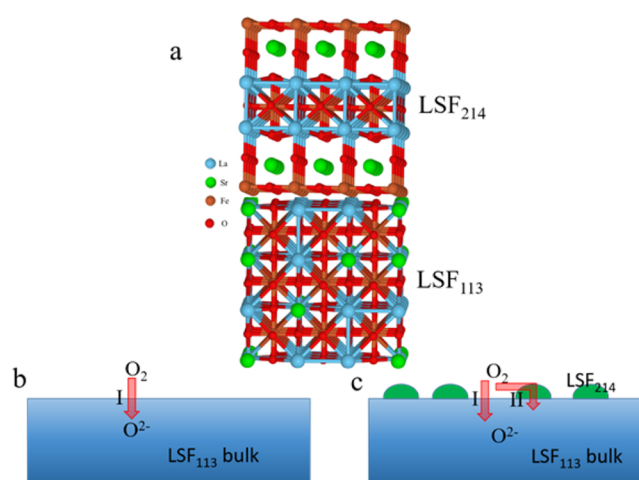

Figure 4. (a) Crystal structure of LSF_{113} and LSF_{214}. Illustration of the oxygen incorporation paths (b) on the single phase LSF_{113} and (c) near the LSF_{214}-LSF_{113} heterointerface.

Oxygen Exchange Rate on LSF_{214}-LSF_{113} Heterointerface. Figure 2 shows the SEM images of LSF_{113} and LSF_{214}-LSF_{113} samples. For the bare LSF_{113} sample, it reveals a dense surface with the grain size ranging from 0.5 to 2 μm (Figure

2a). There are only several isolated holes which are less than 0.3 μm in the cross section as in Figure 2b. After infiltration of $Sr(NO_3)_2$ and the subsequent heat treatment, the surface of
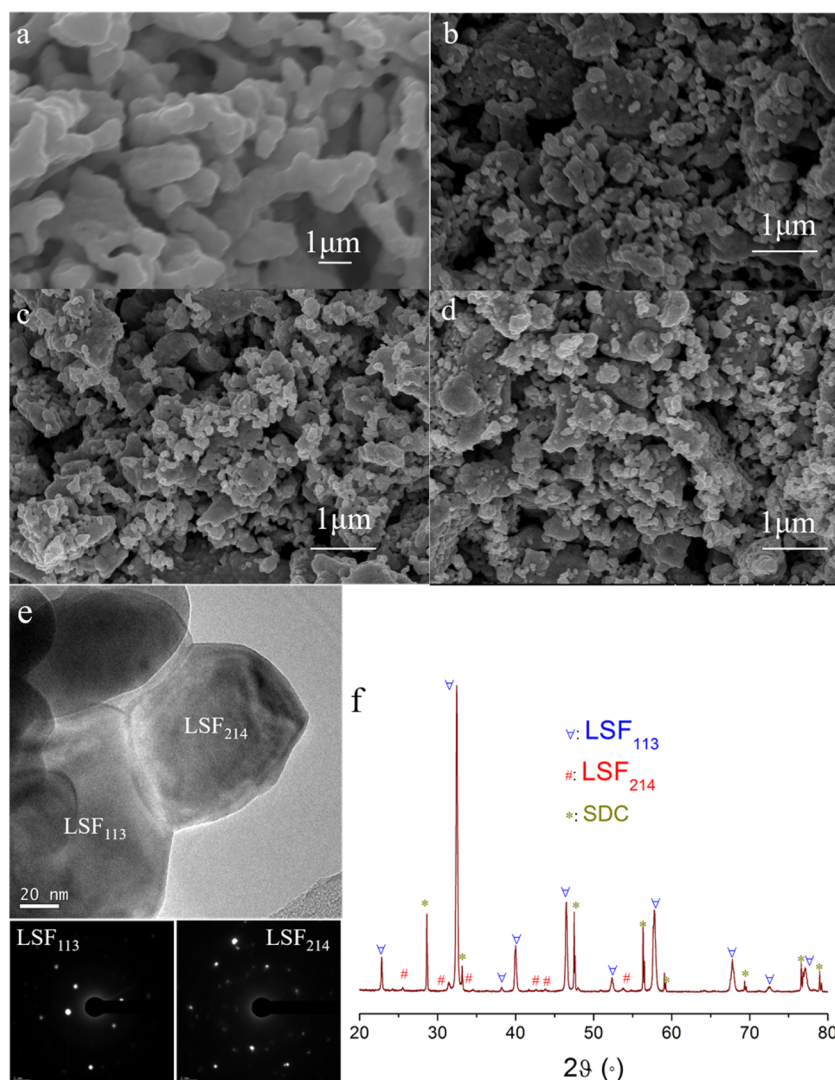
Figure 5. SEM pictures of the cross section: (a) bare LSF$_{113}$ and (b−d) LSF$_{214}$-LSF$_{113}$ electrodes at loading weight of 3.89, 6.49, and 8.75 wt %. TEM and selected area electron diffraction (SAED) of LSF$_{214}$-LSF$_{113}$ heterostructure particle are presented in (e). (f) XRD pattern for 8.75 wt % LSF$_{214}$-LSF$_{113}$ porous electrode (20 μm) supported on SDC electrolyte pellet.

LSF$_{113}$ partially formed a new phase, LSF$_{214}$ nanoislands. These are only isolated LSF$_{214}$ nanoislands on the surface for one time infiltration treatment as shown in Figure 2c. With increasing infiltration time, the LSF$_{214}$ nanoislands became more concentrated, as shown in Figure 2d−f. The AFM images (Figure 2g,h) show the 3D morphology of LSF$_{113}$ surface and LSF$_{214}$ nanoislands surface. LSF$_{113}$ and LSF$_{214}$-LSF$_{113}$ surface are not completely flat with a surface roughness of more than 100 nm. But it still has the possibility of LSF$_{214}$ formed at SrO/SrCO$_3$-LSF$_{113}$ interface due to the unfully crystallized LSF$_{214}$ phase.

The oxygen chemical surface exchange coefficient, K_{chem}, which describes the rate of surface oxygen exchange on the surfaces of LSF$_{113}$ and LSF$_{214}$-LSF$_{113}$ was evaluated by the ECR experiments. At 750 °C, the K_{chem} value of LSF$_{113}$ is 1×10^{-5} cm s^{-1}, obtained by fitting the relaxation time as shown in Figure S3; K_{chem} was 1.5×10^{-5} cm s^{-1} determined by Sogaard et al.[24] using the same method. For the sample with one time infiltration, the K_{chem} value was 2.5×10^{-4} cm s^{-1}, which is 1 order of magnitude higher than the bare LSF$_{113}$ as shown in Figure 3. The K_{chem} value increased to 2.7×10^{-4} and 2.8×10^{-4} cm s^{-1} for the two times and three times infiltrated

samples, respectively. Finally, the K_{chem} value reached the largest value of 4.0×10^{-4} cm s^{-1} for the four times infiltrated sample, consistent with the most concentrated LSF$_{214}$ nanoislands observed in Figure 2f. In order to estimate the relative enhancement in the ORR kinetics near the LSF$_{214}$-LSF$_{113}$ interface compared to the single phase LSF$_{113}$, we computed the enhancement ratio, $K_{214-113chem}/K_{113chem}$, ranging from 13 to 40 at 650−800 °C. The LSF$_{113}$ surface area in the LSF$_{214}$-LSF$_{113}$ samples is smaller than the bare LSF$_{113}$ sample while the K_{chem} values are significantly increased, indicating that the enhanced K_{chem} value must be due to the LSF$_{214}$ nanoislands as observed in the LSF$_{214}$-LSF$_{113}$ samples shown in Figure 2c−f. Nanoislands result in a large number of interfacial boundaries on the LSF$_{214}$-LSF$_{113}$ surface, which are correlated with the enhanced K_{chem} values observed for partial coverage of the LSF$_{214}$ phase on the LSF$_{113}$ surface. The enhanced K_{chem} values of LSF$_{214}$ covered LSF$_{113}$ bulk cannot result from increased oxygen vacancy in the bulk of LSF$_{113}$, suggesting that the presence of LSF$_{214}$-LSF$_{113}$ interfaces on the surface of LSF$_{113}$ is critical to the observed ORR enhancement.

The LSF$_{214}$-LSF$_{113}$ heterostructure with LSF$_{214}$ nanoisland deposited on the LSF$_{113}$ substrate is schematically represented
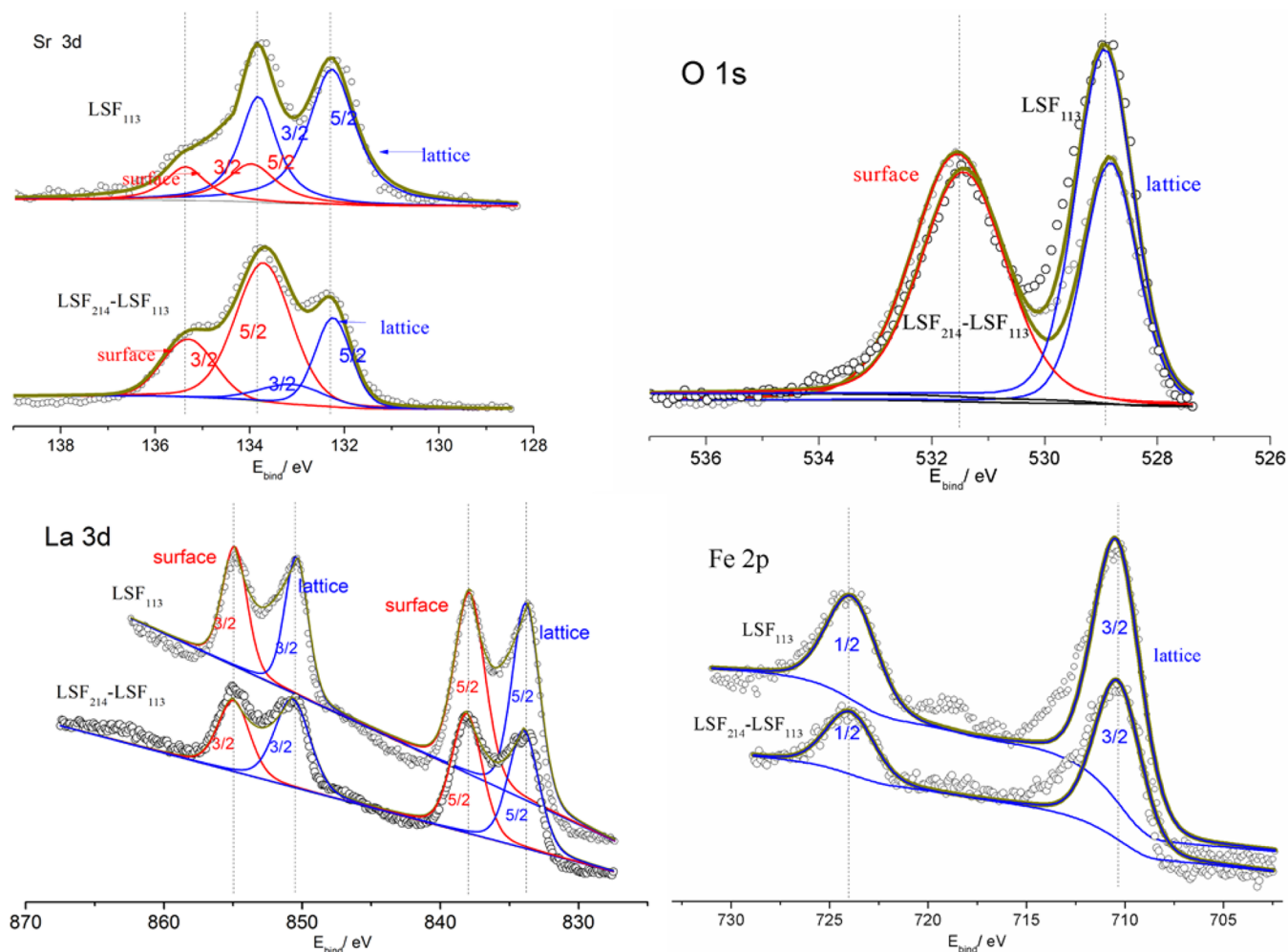
Figure 6. XPS (Sr 3d, O 1s, La 3d, Fe 2p) of LSF_{113} and LSF_{214}-LSF_{113} (8.75 wt %) electrode. Black circles: measured data; yellow line: the sum of fits; gray dotted line: background; and red/blue dotted lines: components. For details about peak fitting and peak assignment see Table S1.
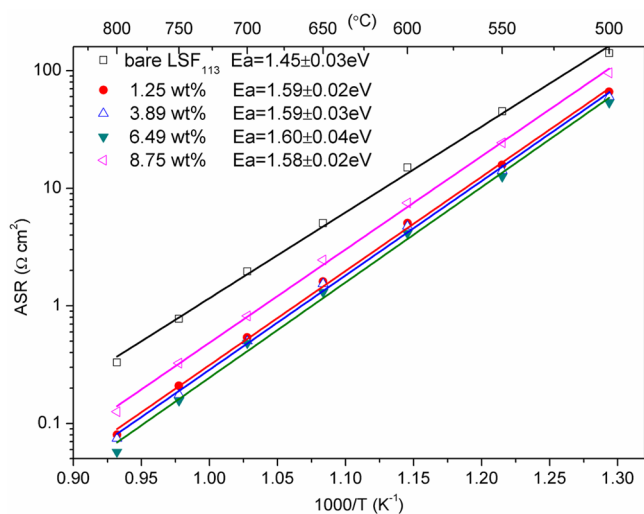

Figure 7. Comparison of the ASR values of the infiltrating weight LSF_{113} cathodes by testing the EIS of symmetric cells.

by a model shown in Figure 4a. The oxygen incorporation path on the single phase LSF_{113} is schematically shown in Figure 4b; O_2 adsorbs onto the LSF_{113} surface and is then dissociated and incorporated by the assistance of a migrating surface oxygen

vacancy. For the LSF_{214}-LSF_{113} heterostructure, there are two parallel paths for oxygen incorporation as schematically shown in Figure 4c, path I and path II. Path I is identical to the oxygen incorporation path of the pure single phase LSF_{113} as shown in Figure 4b. In path II, oxygen adsorbs onto the LSF_{214} surface, dissociates, incorporates, and migrates through the LSF_{214} onto the LSF_{113}. Path II starts with the O_2 adsorption on the LSF_{214} surface followed by eventual diffusion of O^{2-} along the LSF_{214}-LSF_{113} heterostructure. The diffusion is enhanced in the present case since the R−P phase has a higher oxygen surface exchange coefficient than the perovskite phase.[12,25,26]

In addition to surface effects of heterostructues, strain effects have been shown to induce an enhancement in the oxygen incorporation at heterointerface as reported by Yildiz et al.[27] As discussed above, the lattice parameters between LSF_{113} and LSF_{214} have a significant change in both a and c, from 5.547 and 7.821 Å to 3.852 and 12.751 Å, respectively. 31% and 63% mismatch in lattice a and c are expected to result in significant tensile strain. Oxygen dissociation and incorporation kinetics are limited by the availability and mobility of oxygen vacancies on the perovskite cathode surface.[27−29] In the LSF_{214}-LSF_{113} heterostructure, as the tensile strain increases up to the limit of the elastic stretching, both the oxygen molecule adsorption and oxygen vacancy formation become more favored.[28] Oxygen vacancies are more favorably formed due to the weakening of
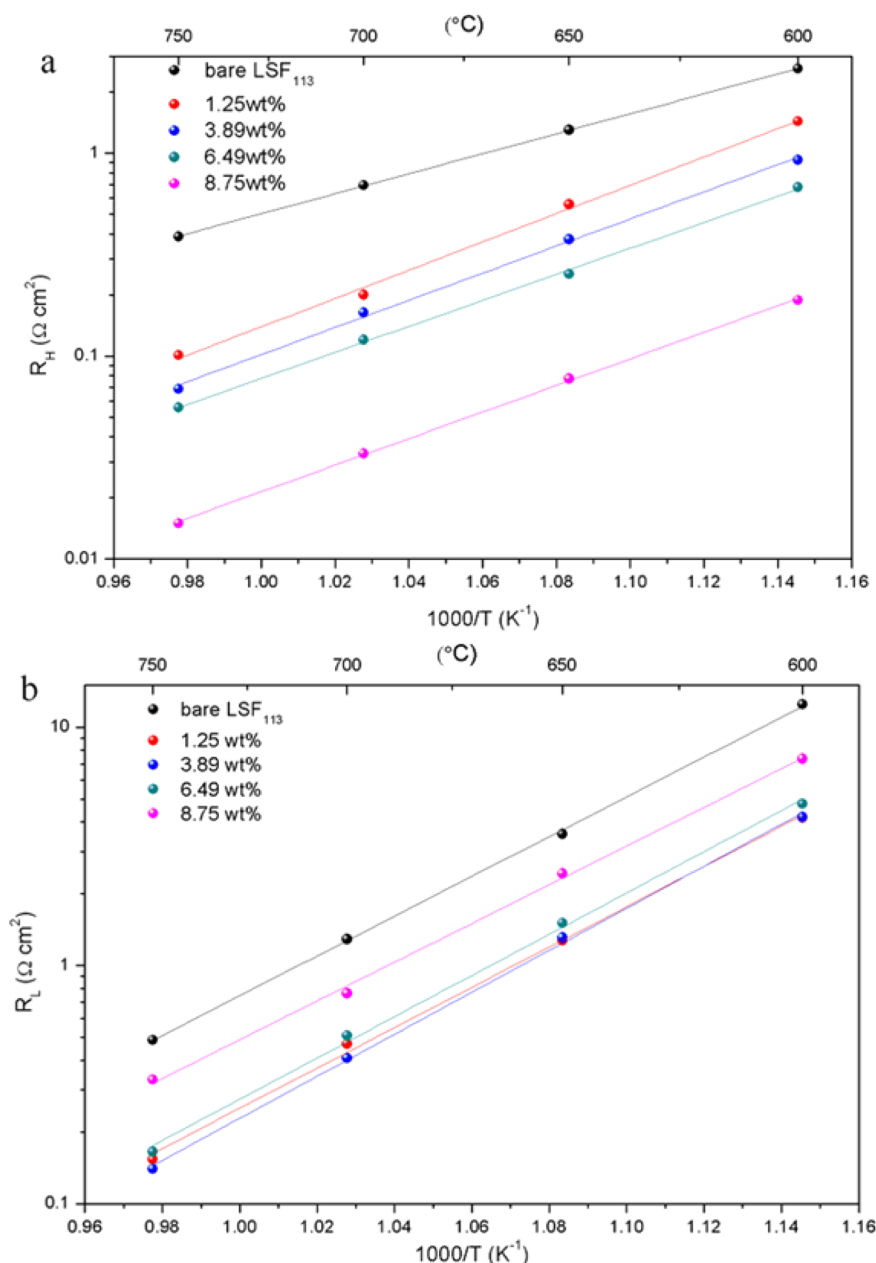
Figure 8. Comparing of (a) high frequency resistance and (b) low frequency resistance of LSF_{214}-LSF_{113} derived from impedance spectra fitting.

the in-plane Fe−O bonds upon tensile strain.[27] The energy barrier for oxygen vacancy migration on LSF_{113} will be significantly lowered with the increase of strain because of the increased space available in the migration path of oxygen. Since the perovskite LSF_{113} conducts oxygen ions via oxygen vacancies while the LSF_{214} tolerates oxygen in interstitial positions, O^{2-} ion redistribution in the LSF_{214}-LSF_{113} heterostructure could enhance the charge carrier concentration in the boundary zones.

Characterization and Electrochemical Performance of LSF_{214}-LSF_{113} Electrode. In the LSF_{113} cathode scaffold, infiltration with $Sr(NO_3)_2$ resulted in a thin LSF_{214} layer on the LSF_{113} scaffold surface. Figure 5a shows the typical microstructure of bare LSF_{113} electrodes with the particle size of 1−3 μm. While for LSF_{214}-LSF_{113} electrodes (Figure 5c,d), more LSF_{214} was formed on LSF_{113} frame with the increased loading weight from 3.89 to 8.75 wt %. Figure 5e shows the TEM image

of the heterostructure LSF_{214}-LSF_{113} particle as well as the selected area electron diffraction results of LSF_{113} and LSF_{214}. The SAED image of LSF_{214} and LSF_{113} confirms the formation of LSF_{214} nanoparticle (about 80 nm) on the support of LSF_{113} frame. Figure 5f gives the XRD pattern of porous 8.75 wt % LSF_{214}-LSF_{113} electrode (20 μm) supported on SDC electrolyte pellet. Besides the SDC peaks (as supporting pellet), the others peaks are attributed to LSF_{113} or LSF_{214} phase. LSF_{113} as electrode frame is the majority phase and LSF_{214} nanoparticles formed on LSF_{113} frame is the minority phase which is consistent with XRD peaks intensity.

XPS spectra of Sr 3d, O 1s, La 3d, and Fe 2p of baseline LSF_{113} and LSF_{214}-LSF_{113} electrodes are shown in Figure 6. The La, Sr, Fe, and O peaks of the base LSF_{113} can be fitted to a LSF_{113} lattice component at lower binding energy, E_{bind}, and to a surface related component with a higher E_{bind}.[30] As revealed from the XRD and SEM study, there will be a layer of LSF_{214}
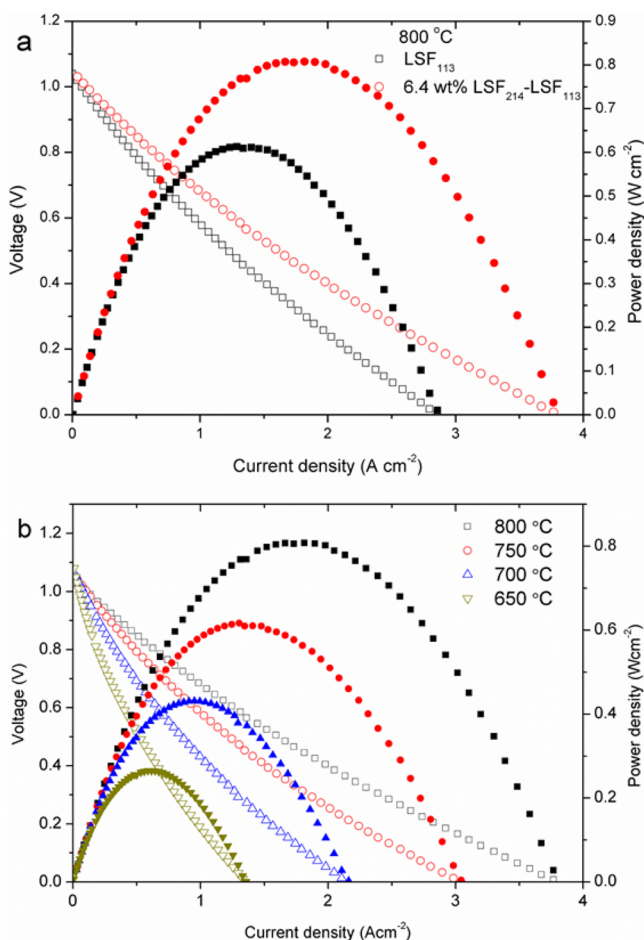
Figure 9. (a) $V-I$ performance measured at 800 °C for anode-supported single cells with LSF_{113} and 6.4 wt % LSF_{214}-LSF_{113} cathodes and (b) cell performance of LSF_{214}-LSF_{113} cathodes at 650−800 °C.

formed on the LSF_{113} scaffold surface. After surface formation of LSF_{214}, the XPS spectra of La and Fe demonstrated almost no shift in peak position. The XPS spectra of the surface Sr and O components in the LSF_{214}-LSF_{113} sample exhibited much higher intensities relative to the lattice components in comparison to the base LSF_{113}. The Sr 3d peak was found to exhibit three unique features, which could be fitted by two sets of Sr $3d_{5/2}$ and $3d_{3/2}$ doublets with an energy separation, while for LSF_{214}-LSF_{113} the intensity of high-energy set of Sr 3d was found to increase in comparison to those of the low-energy set. The increase in the contribution from surface species should be due to the LSF_{214} phase that has been formed on the surface and has higher binding energy in Sr. The XPS result indicates the outer layer deposition of LSF_{214} in the LSF_{214}-LSF_{113} heterostructure, which is consistent with the TEM result. The atomic concentrations and binding energy of La, Sr, Fe, and O for LSF_{113} and LSF_{214}-LSF_{113} electrode are shown in Table S1.

The electrocatalytic activity toward ORR on the LSF_{113} and LSF_{214}-LSF_{113} electrode was evaluated by electrochemical impedance spectroscopy. Figure 7 shows the area specific resistance of LSF_{113} and LSF_{214}-LSF_{113} cathode with the SDC electrolyte. The ASR values dramatically decreased after infiltration of $Sr(NO_3)_2$ that created a layer of LSF_{214} in the LSF_{113} scaffold. At 750 °C, the ASR value for bare LSF_{113} was 0.775 Ω cm^2, while after infiltrated with 1.25 and 3.89 wt % of

$Sr(NO_3)_2$, it was only 0.209 and 0.175 Ω cm^2 for the LSF_{214}-LSF_{113} electrode. At 6.49 wt % infiltration load, the lowest ASR value, 0.156 Ω cm^2, was achieved, which was only 20.1% of the original value. Further infiltration caused an increase of the ASR value. For example, at 8.75 wt % infiltration load, the ASR value was 0.325 Ω cm^2. As revealed in SEM images, it is the higher coverage of LSF_{214} phase that cause the change in LSF_{214}-LSF_{113} electrode ASR value.

To evaluate what is responsible for the observed ORR enhancement, impedance spectra were analyzed to evaluate factors that may influence the ORR kinetics. Figure S4 shows the fitting result of impedance spectra at 600−750 °C with an equivalent circuit of $LR_b(R_iCPE_i)$ using the Zview program. The physical meaning of each element in the equivalent circuit has been explained in our prior publication.[31] In the impedance analysis, the impedance spectra could be represented by two arcs as the high frequency and low frequency arc. Figure 8 displays the high frequency resistance R_H and low frequency resistance R_L. In Figure 8a, the R_H values of the infiltrated electrodes were lower than the bare LSF_{113} electrode. For example, at 700 °C, the R_H value of bare LSF_{113} was 0.694 Ω cm^2, while it decreased to 0.201 and 0.164 Ω cm^2 for the LSF_{214}-LSF_{113} electrode at 1.25 and 6.49 wt % infiltration loading. The lowest ASR value obtained in this work was 0.03 Ω cm^2 at 8.75 wt % loading. For the low frequency resistance R_L at 700 °C, it was 1.291 Ω cm^2 for the bare LSF_{113}.

The oxygen reduction reaction in a SOFC cathode is a complex process where oxygen molecules go through adsorption, dissociation, and formation of oxygen ions on the surface of a mixed oxygen ionic and electronic conducting cathode, followed by oxygen ionic transport in the bulk of the cathode. Our study indicates that formation of LSF_{214} on the LSF_{113} surface can drastically enhance the oxygen surface exchange coefficient, resulting in acceleration of the oxygen incorporation process and formation of additional oxygen ions at the LSF_{214}-LSF_{113} cathode. An analysis of the impedance spectra indicates the R_H value decreases with increased formation of LSF_{214} on the LSF_{113} surface. It is commonly accepted that in the LSF_{113} cathode R_H represents the oxygen ionic transport process in the electrode. For the bare LSF_{113} electrode, oxygen can transport through both the surface and the bulk in LSF_{113}. After decoration with LSF_{214} on the LSF_{113} surface, oxygen transport process was greatly accelerated due to the larger D_{chem} value of R−P phase than LSF_{113} perovskite phase[24−26] in the bulk transport pathway. In addition, oxygen species that move along the surface of LSF_{214} must be faster than in LSF_{113}. Therefore, for the LSF_{214}-LSF_{113} heterostructure electrode, more LSF_{214} results in smaller R_H values.

It has been shown that LSF_{214} can drastically enhance the oxygen incorporation process into the LSF_{113} bulk. Generally, the low frequency response for the LSF_{113}-based electrode is related to the charge transfer process, which may include steps such as adsorption and dissociation of oxygen molecules and electron transfer to form oxygen ions. The significant reduction in R_L by LSF_{214} demonstrates substantial increase in the kinetics for the surface steps of the cathode reaction. R_L reduction is consistent with K_{chem} enhancement, which has demonstrated significant increase in the oxygen incorporation rate.

The performance of the LSF_{214}-LSF_{113} cathode in SOFC was further evaluated with YSZ-Ni anode supported YSZ/SDC (10/2 um) electrolyte single cell, shown in Figure S5. As shown in Figure 9a, the peak power density for the cell with LSF_{113} cathode was 0.61 W cm^{-2} but increased by 33.3% to 0.81 W

cm^{-2} with 6.4 wt % LSF$_{214}$-LSF$_{113}$ cathode. The performance data for this configuration (6.4 wt % LSF$_{214}$-LSF$_{113}$ cathode) is shown in Figure 9b where peak power densities at 800, 750, 700, and 650 °C were 0.81, 0.62, 0.43, and 0.26 W cm^{-2}, respectively.

CONCLUSION

This study illustrates the potential of utilizing heterostructured oxide surfaces/interfaces to develop highly active surface oxygen exchange materials for applications in the field of solid-state electrochemical devices. 3D LSF$_{214}$-LSF$_{113}$ heterostructured electrodes fabricated by simple infiltration has provided an elegant and low cost novel approach to improve the performance of SOFC cathodes. The oxygen surface exchange coefficient of LSF$_{113}$ could be enhanced up to 1 order of magnitude by the formation of LSF$_{214}$ nanoislands on the LSF$_{113}$ surface. The higher catalytic activity of LSF$_{214}$ and mismatch in lattice parameter between LSF$_{214}$ and LSF$_{113}$ regions contributed to the observed ORR enhancement. Fuel cell tests with the LSF$_{214}$-LSF$_{113}$ electrode indicated that the polarization resistance could be greatly reduced due to the enhanced oxygen transport process and accelerated oxygen incorporation rate by LSF$_{214}$ in LSF$_{113}$ electrode scaffold. The current study represents a promising general strategy to improve the performance of SOFC cathodes.

ASSOCIATED CONTENT

Ⓢ Supporting Information

The Supporting Information is available free of charge on the ACS Publications website at DOI: 10.1021/acsami.6b14625.

Characterization of LSF$_{113}$ and LSF$_{214}$ phase by XRD Rietveld refinement and thermogravimetric analysis; oxygen surface exchange kinetic of different LSF$_{214}$ loading weight, detailed study of X-ray photoelectron spectroscopy and electrochemical analysis for LSF$_{214}$-LSF$_{113}$electrode, and SEM images for full cell morphology (PDF)

AUTHOR INFORMATION

Corresponding Author

*Tel ++86-551-63607475; Fax ++86-551-63601592; e-mail xiacr@ustc.edu.cn (C.X.).

ORCID Ⓘ

Changrong Xia: 0000-0002-4254-1425

Notes

The authors declare no competing financial interest.

ACKNOWLEDGMENTS

REFERENCES

(1) Ormerod, R. M. Solid Oxide Fuel Cells. *Chem. Soc. Rev.* **2003**, *32* (1), 17−28.

(2) Adler, S. B. Factors Governing Oxygen Reduction in Solid Oxide Fuel Cell Cathodes. *Chem. Rev.* **2004**, *104* (10), 4791−4844.

(3) Peng, R.; Wu, T.; Liu, W.; Liu, X.; Meng, G. Cathode Processes and Materials for Solid Oxide Fuel Cells with Proton Conductors as Electrolytes. *J. Mater. Chem.* **2010**, *20* (30), 6218−6225.

(4) Pena, M.; Fierro, J. Chemical Structures and Performance of perovskite oxides. *Chem. Rev.* **2001**, *101* (7), 1981−2018.

(5) Guo, X.; Maier, J. Ionically Conducting Two-Dimensional Heterostructures. *Adv. Mater.* **2009**, *21* (25−26), 2619−2631.

(6) Dulli, H.; Dowben, P.; Liou, S.-H.; Plummer, E. Surface Segregation and Restructuring of Colossal-Magnetoresistant Manganese Perovskites La$_{0.65}$Sr$_{0.35}$MnO$_3$. *Phys. Rev. B: Condens. Matter Mater. Phys.* **2000**, *62* (22), R14629.

(7) Garcia-Barriocanal, J.; Rivera-Calzada, A.; Varela, M.; Sefrioui, Z.; Iborra, E.; Leon, C.; Pennycook, S. J.; Santamaria, J. Colossal Ionic Conductivity at Interfaces of Epitaxial ZrO$_2$: Y$_2$O$_3$/SrTiO$_3$ Heterostructures. *Science* **2008**, *321* (5889), 676−680.

(8) Sata, N.; Eberman, K.; Eberl, K.; Maier, J. Mesoscopic Fast Ion Conduction in Nanometre-Scale Planar Heterostructures. *Nature* **2000**, *408* (6815), 946−949.

(9) Mutoro, E.; Crumlin, E. J.; Biegalski, M. D.; Christen, H. M.; Shao-Horn, Y. Enhanced Oxygen Reduction Activity on Surface-Decorated Perovskite Thin Films for Solid Oxide Fuel Cells. *Energy Environ. Sci.* **2011**, *4* (9), 3689−3696.

(10) Crumlin, E. J.; Mutoro, E.; Ahn, S.-J.; la O', G. J.; Leonard, D. N.; Borisevich, A.; Biegalski, M. D.; Christen, H. M.; Shao-Horn, Y. Oxygen Reduction Kinetics Enhancement on a Heterostructured Oxide Surface for Solid Oxide Fuel Cells. *J. Phys. Chem. Lett.* **2010**, *1* (21), 3149−3155.

(11) Sase, M.; Yashiro, K.; Sato, K.; Mizusaki, J.; Kawada, T.; Sakai, N.; Yamaji, K.; Horita, T.; Yokokawa, H. Enhancement of Oxygen Exchange at the Hetero Interface of (La, Sr)CoO$_3$/(La, Sr)$_2$CoO$_4$ in Composite Ceramics. *Solid State Ionics* **2008**, *178* (35), 1843−1852.

(12) Sase, M.; Hermes, F.; Yashiro, K.; Sato, K.; Mizusaki, J.; Kawada, T.; Sakai, N.; Yokokawa, H. Enhancement of Oxygen Surface Exchange at the Hetero-Interface of (La, Sr)CoO$_3$/(La, Sr)$_2$CoO$_4$ with PLD-Layered Films. *J. Electrochem. Soc.* **2008**, *155* (8), B793−B797.

(13) Ahn, S. J.; Crumlin, E.; Orikasa, Y.; Biegalski, M. D.; Christen, H. M.; Shao-Horn, Y. Catalytic Activity Enhancement for Oxygen Reduction on Epitaxial Perovskite Thin Films for Solid-Oxide Fuel Cells. *Angew. Chem., Int. Ed.* **2010**, *49* (31), 5344−5347.

(14) Gadre, M. J.; Lee, Y.-L.; Morgan, D. Cation Interdiffusion Model for Enhanced Oxygen Kinetics at Oxide Heterostructure Interfaces. *Phys. Chem. Chem. Phys.* **2012**, *14* (8), 2606−2616.

(15) Sun, Y.-K.; Myung, S.-T.; Kim, M.-H.; Prakash, J.; Amine, K. Synthesis and Characterization of Li-[(Ni$_{0.8}$Co$_{0.1}$Mn$_{0.1}$)$_{0.8}$(Ni$_{0.5}$Mn$_{0.5}$)$_{0.2}$]O$_2$ with the Microscale Core-Shell Structure as the Positive Electrode Material for Lithium Batteries. *J. Am. Chem. Soc.* **2005**, *127* (38), 13411−13418.

(16) Song, H. S.; Hyun, S. H.; Kim, J.; Lee, H.-W.; Moon, J. A Nanocomposite Material for Highly Durable Solid Oxide Fuel Cell Cathodes. *J. Mater. Chem.* **2008**, *18* (10), 1087−1092.

(17) Hong, T.; Zhang, L.; Chen, F.; Xia, C. Oxygen Surface Exchange Properties of La$_{0.6}$Sr$_{0.4}$Co$_{0.8}$Fe$_{0.2}$O$_{3-\delta}$ Coated with Sm$_x$Ce$_{1-x}$O$_{2-\delta}$. *J. Power Sources* **2012**, *218*, 254−260.

(18) Lane, J.; Kilner, J. Measuring Oxygen Diffusion and Oxygen Surface Exchange by Conductivity Relaxation. *Solid State Ionics* **2000**, *136*, 997−1001.

(19) Szot, K.; Speier, W. Surfaces of Reduced and Oxidized SrTiO$_3$ from Atomic Force Microscopy. *Phys. Rev. B: Condens. Matter Mater. Phys.* **1999**, *60* (8), 5909.

(20) Jennings, A.; Skinner, S.; Helgason, Ö. Structural Properties of La$_x$Sr$_{2-x}$FeO$_{4\pm\delta}$ at High Temperature and Under Reducing Conditions. *J. Solid State Chem.* **2003**, *175* (2), 207−217.

(21) Jennings, A.; Skinner, S. Thermal Stability and Conduction Properties of the La$_x$Sr$_{2-x}$FeO$_{4+\delta}$ System. *Solid State Ionics* **2002**, *152*, 663−667.

(22) Omata, T.; Ueda, K.; Hosono, H.; Katada, M.; Ueda, N.; Kawazoe, H. Electrical and Magnetic Properties of Hole-Doped

$Sr_{1+x}La_{1+x}FeO_4$. *Phys. Rev. B: Condens. Matter Mater. Phys.* **1994**, *49* (15), 10194.

(23) Li, M.; Wang, Y.; Wang, Y.; Chen, F.; Xia, C. Bismuth Doped Lanthanum Ferrite Perovskites as Novel Cathodes for Intermediate-Temperature Solid Oxide Fuel Cells. *ACS Appl. Mater. Interfaces* **2014**, *6* (14), 11286−11294.

(24) Søgaard, M.; Hendriksen, P. V.; Mogensen, M. Oxygen Nonstoichiometry and Transport Properties of Strontium Substituted Lanthanum Ferrite. *J. Solid State Chem.* **2007**, *180* (4), 1489−1503.

(25) Kim, G.; Wang, S.; Jacobson, A.; Chen, C. Measurement of Oxygen Transport Kinetics in Epitaxial $La_2NiO_{4+\delta}$ Thin Films by Electrical Conductivity Relaxation. *Solid State Ionics* **2006**, *177* (17), 1461−1467.

(26) Ivanov, D.; Pinaeva, L.; Isupova, L.; Sadovskaya, E.; Prosvirin, I.; Gerasimov, E. Y.; Yakovleva, I. Effect of Surface Decoration with $LaSrFeO_4$ on Oxygen Mobility and Catalytic Activity of $La_{0.4}Sr_{0.6}FeO_{3-\delta}$ in High-Temperature N_2O Decomposition, Methane Combustion and Ammonia Oxidation. *Appl. Catal., A* **2013**, *457*, 42−51.

(27) Han, J. W.; Yildiz, B. Mechanism for Enhanced Oxygen Reduction Kinetics at the $(La, Sr)CoO_3/(La, Sr)_2CoO_4$ Hetero-Interface. *Energy Environ. Sci.* **2012**, *5* (9), 8598−8607.

(28) Han, J. W.; Yildiz, B. Enhanced One Dimensional Mobility of Oxygen on Strained $LaCoO_3$ (001) Surface. *J. Mater. Chem.* **2011**, *21* (47), 18983−18990.

(29) Mastrikov, Y. A.; Merkle, R.; Heifets, E.; Kotomin, E. A.; Maier, J. Pathways for Oxygen Incorporation in Mixed Conducting Perovskites: A DFT-Based Mechanistic Analysis for $(La, Sr)MnO_{3-\delta}$. *J. Phys. Chem. C* **2010**, *114* (7), 3017−3027.

(30) Van Der Heide, P. Systematic X-ray Photoelectron Spectroscopic Study of $La_{1-x}Sr_x$-Based Perovskite-Type Oxides. *Surf. Interface Anal.* **2002**, *33* (5), 414−425.

(31) Jiang, Z.; Zhang, L.; Cai, L.; Xia, C. Bismuth Oxide-Coated $(La,Sr)MnO_3$ Cathodes for Intermediate Temperature Solid Oxide Fuel Cells with Yttria-Stabilized Zirconia Electrolytes. *Electrochim. Acta* **2009**, *54* (11), 3059−3065.